

Hopping mechanism for superconductivity revealed by Density Functional Theory

Jose A. Alarco¹ and Ian D. R. Mackinnon²

Queensland University of Technology, Brisbane, QLD 4001, Australia

Email: ian.mackinnon@qut.edu.au

¹ORCID: 0001-6345-071X; ²ORCID: 0002-0732-8987

Keywords: Magnesium diboride, tight binding equations, Fermi surfaces, nesting, band structures, cosine bands, degenerate bands

Cosine-shaped bands that occur in DFT-based electronic band structures for MgB₂ are further analysed with calculations along reciprocal directions parallel to the high symmetry Γ -A direction at regular intervals along Γ -M. Band degeneracies in close proximity to the Fermi surface (i.e. offset from Γ -A), do not emulate the degenerate bands along Γ -A. At the Fermi surface, bands split and align favourably for electron-hole pairing with the nodal inflection point located at the Fermi level. Tight-binding equations, including corrections to describe the observed asymmetry of a cosine-shaped band, can be compared to the secular equation obtained for Bloch orbitals of an infinite linear chain of atoms with two s-states. These equations show unequivocally that a hopping mechanism is associated with the cosine-shaped band asymmetry; an asymmetry strongly correlated with the superconducting gap and Fermi surface nesting. Intersections of folded Fermi-surfaces and electronic band crossings provide avenues or 'pathways' for electrons from the nested collection to drastically change velocity or momentum, resulting in scattering and disruption of nested, coherent behaviour. Determination of cosine band asymmetry, also established for other two element superconductors such as CaC₆ and LaH₁₀, is relevant for interpretation of superconductivity mechanisms in many other multi-element compounds.

1. Introduction

The importance of sigma (σ) bands for the superconductivity of MgB₂ was established soon after discovery of superconductivity in this compound, largely through use of density functional theory (DFT) calculations.^[1] Even though the connection between the associated dynamic bond deformations and modes of vibration was established with optical vibration modes^[2, 3], similar results are expected for the dynamic σ bond deformations associated with acoustic vibration modes, since electron density redistributes to balance the modified forces.^[4] Additional important correlations between the σ bands and σ Fermi surfaces, phonon anomalies and superconducting transition temperatures (T_c), or gap energies, were subsequently investigated using high resolution DFT calculations.^[5] Correlations have been established which conform well with experimentally determined values for elemental cation substitution,^[6] bond electron density modulations^[4] and external pressure dependence^[7], particularly when the calculation resolution was higher (for a smaller Δk -grid) than the minimum distance between adjacent σ Fermi surfaces.^[8]

Understanding the orbital character of hybridised bonds combined with the electronic properties of a compound is essential for explanations of physical properties,^[9] and critical for the design and synthesis of new compounds with targeted properties.^[10, 11] Knowledge of bond orbital character, reflected in electronic band structures, helps to bridge the physics with the chemistry of solid-state materials. Experimental observations of superlattice character in MgB₂ using Raman spectroscopy^[12] and with synchrotron THz spectroscopy^[13] led to an examination of the P6/mmm symmetry typically attributed to MgB₂ based on atomic positions.^[14] The bonding and antibonding character of bands and orbitals are key features that provide a more detailed, and nuanced, indication of superlattice symmetry that is often overlooked, or indeterminate, in dynamic systems.^[5, 13]

The introduction of a bandgap at the Fermi level can lower the energy of a metal.^[15-18] This generally happens in two typical ways; one leads to formation of a charge density wave (CDW) state and the other, to formation of a superconducting state.^[15] In both cases, the lowering of energy involves interaction of occupied states with unoccupied states lying close to the Fermi level. However, these states differ in the way they interact. A metal-to-insulator phase transition takes place during formation of a CDW, while a metal-to-superconductor phase transition is induced in the other case. Interband pair-state excitations become favourable when two Fermi surfaces are very similar, or nested, and when the metal has a large average phonon frequency $\langle \omega \rangle$.^[15] If more than one partially-filled band is present, a superconductor with T_c well above the McMillan limit is often explained as due to a “multiband” mechanism, while remaining

within the confines of the BCS theory for superconductivity.^[15] From the viewpoint of one-electron band theory, a superconducting state also involves orbital mixing among band levels above and below the Fermi level.^[10]

Band structure calculations on condensed matter systems with electrons strongly bound to each atom are commonly ascribed to a tight binding model.^[13, 18, 19] The σ bands and Fermi surfaces in the electronic band structure of MgB₂ (and of other superconductors) contain approximately cosine shaped bands and Fermi surface cross-sections that are associated with tight binding equations. Hopping integrals, also known as transfer coefficients, are essential parameters in tight binding equations. Many hopping models have been created to explain superconductivity, particularly for the high T_c cuprates.^[20, 21] Such models become more powerful when informed by parameters extracted from DFT calculations, since these calculations deal with collective charges, or quasiparticles, instead of electrons. In this context, DFT provides a direct link between crystal structure and material properties.^[22]

This article provides context, and places into perspective, our DFT calculations on electronic band structures for MgB₂ as an exemplar for which approximately cosine shaped bands are described by tight binding equations. Equations for associated electronic bands and Fermi surfaces, (including the respective band and Fermi surface topologies), are provided that meet the requirements for, and correspond to, a hopping mechanism for superconductivity.

2. Results

The following examples show how high symmetry directions can lead to misinterpretation of band degeneracies when it is assumed that the physics at, or near, the Fermi surface closely resembles that of electrons in bands along those directions. A sequence of examples is further discussed in Section 4.

2.1. Band structures at 0 GPa

Based on earlier calculations and experimental data,^[5, 12, 13] we utilise a superlattice, doubled along the c -axis direction with space group $P\bar{6}c2$, to elucidate key features of the MgB₂ band structure. **Figure 1a** shows the electronic band structure for MgB₂ at 0 GPa calculated along high symmetry reciprocal directions using the GGA functional. The Γ -A region (red outline) is the focus of this work. Reciprocal directions for the $2c$ superlattice are shown in **Figure 1b**.

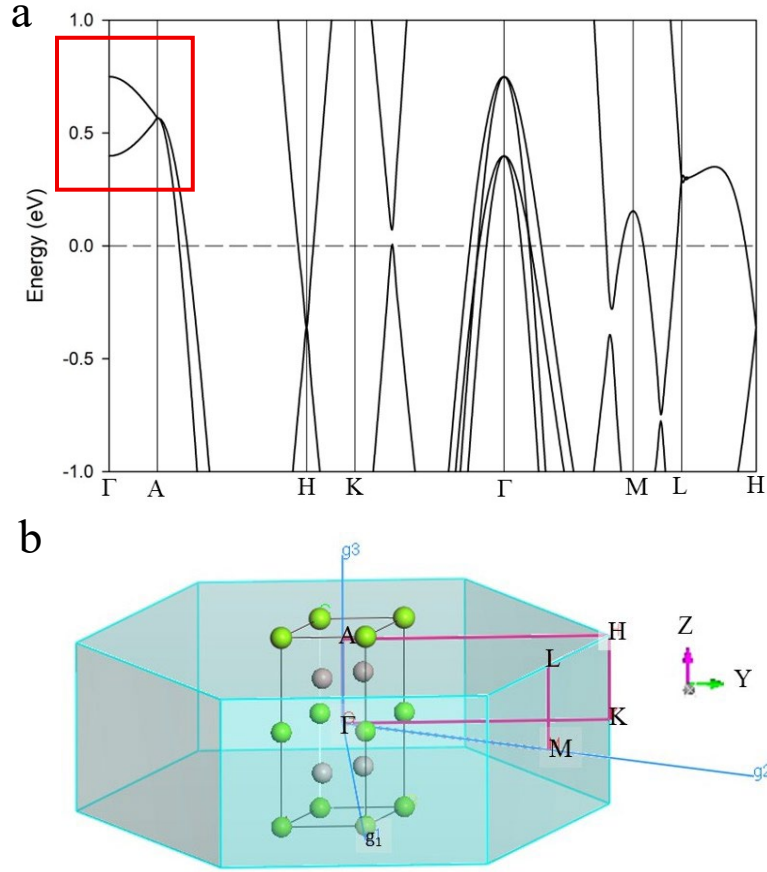


Figure 1. (a) Electronic band structure for the $2c$ superlattice of MgB_2 at 0 GPa calculated along high symmetry directions. The Γ – A region (red outline) is the focus of this work. (b) reciprocal space orientations for the $2c$ MgB_2 superlattice.

Figure 2 shows key segments of the EBS for the MgB_2 superlattice at Γ – A and Γ – M as well as for directions parallel to Γ – A at regular intervals along the Γ – M direction. These segments sample the band structure at intervals within the Brillouin zone that approximate nodal inflection points for light and heavy effective mass σ bands. The approximate loci of inflection points, between $(0, k_y, 0)$ and $(0, k_y, 0.5)$ are obtained from calculations previously published for $k_F^{H,L}$.^[5, 12] The value and derivation of ΔE_{gap} (at 7.9 meV) shown for the Γ – A section in Figure 2a is described in detail in an earlier publication.^[5] At $k_y = 0.097$, the degenerate bands along Γ – A split into two separate bands that cross near E_F with an overlap at Γ of 29.0 meV. For this calculation series, the overlap at Γ reduces to 1.3 meV within ± 1.0 meV of E_F for $k_y = 0.101$. Similar calculations undertaken using the GGA functional are shown in Supporting Information (**Figure S1**).

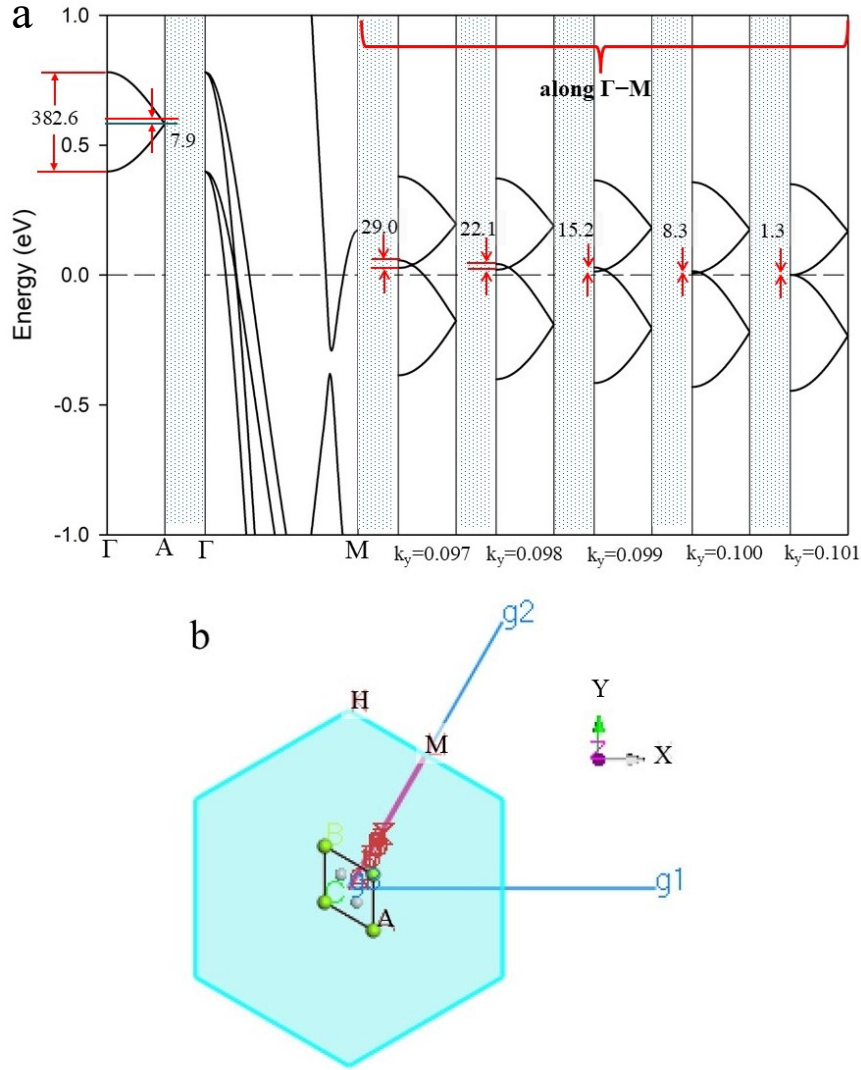


Figure 2. (a) EBS of a $2c$ superlattice for MgB_2 at 0 GPa calculated using the LDA functional along reciprocal directions parallel to Γ -A direction and intersecting along Γ -M at approximate nodal inflection points for the light and heavy effective mass σ bands (i.e. at $(0, k_y, 0)$ and $(0, k_y, 0.5)$). Energy values for bands at Γ -A and Γ -M are in meV; values for k_y are shown at bottom of plot for each segment along Γ -M. (b) reciprocal space orientations for the $2c$ superlattice of MgB_2 showing the k_y intersections along Γ -M used to generate data points in (a).

2.1.1. Corresponding Fermi surfaces

Figure 3a shows Fermi surfaces for the light and heavy effective mass quasiparticles of σ bands in the $2c$ superlattice for MgB_2 at 0 GPa. The region between the inner tubular sections of the Fermi surface (parallel to Γ -A) and the outer shaded section highlight the extent and shape of these warped cylinders^[23] of σ bands. At zero temperature, these regions represent states

populated with electrons or with empty states for the light and heavy effective masses for the same \mathbf{k} vector, respectively.

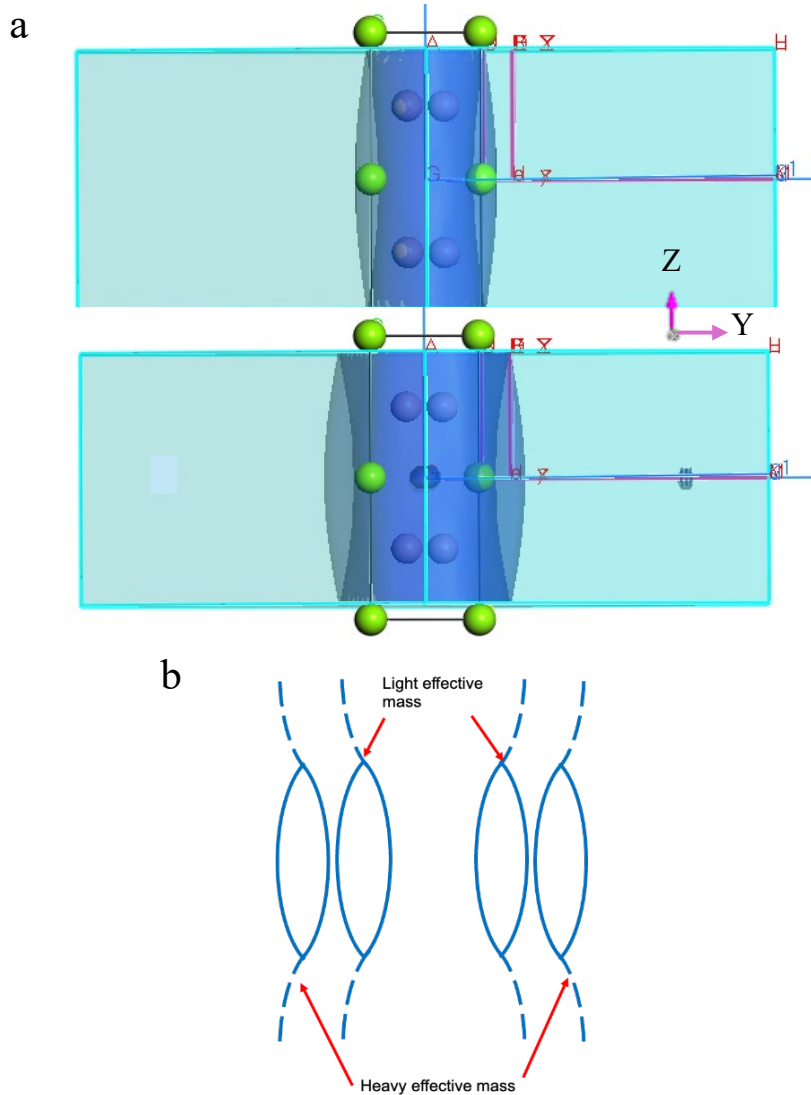


Figure 3. (a) Fermi surfaces for the light and heavy effective mass σ bands of the $2c$ superlattice for MgB_2 at 0 GPa. (b) Schematic of the projected warped tubular Fermi surfaces for a single MgB_2 unit cell and the folded bands for the $2c$ superlattice.

Figure 3b is a schematic highlighting the origin of Fermi surfaces for the $2c$ superlattice of MgB_2 by folding the single primitive cell Fermi surface. The bands displayed in Figure 2a have been calculated along a reciprocal direction that approximately lies between the two lens shaped projections of the folded cosine bands in Figure 3b. Note that the folded light and heavy effective mass Fermi surfaces do not intersect at 0 GPa.

2.2. Band structures at high pressure

Figure 4 shows the electronic band structures of the $2c$ superlattice for MgB_2 calculated parallel to the Γ - A axis (at regular intervals along Γ - M) at 4 GPa and 8 GPa, respectively, using the

LDA functional. Calculations for these samplings along Γ -M follow the same procedure as indicated for Figure 2a. Similar to the case for 0 GPa, the separated light and heavy σ bands cross in proximity to the Fermi level with greater overlap at Γ compared to that in Figure 2a. At 8 GPa (Figure 4b), this trend for band splitting near E_F continues with greater overlap of the light and heavy bands at Γ . At 4 GPa and 8 GPa, the Fermi level intersects the lower band at $k_y = 0.097$ and at $k_y = 0.101$ intersects the higher energy band.

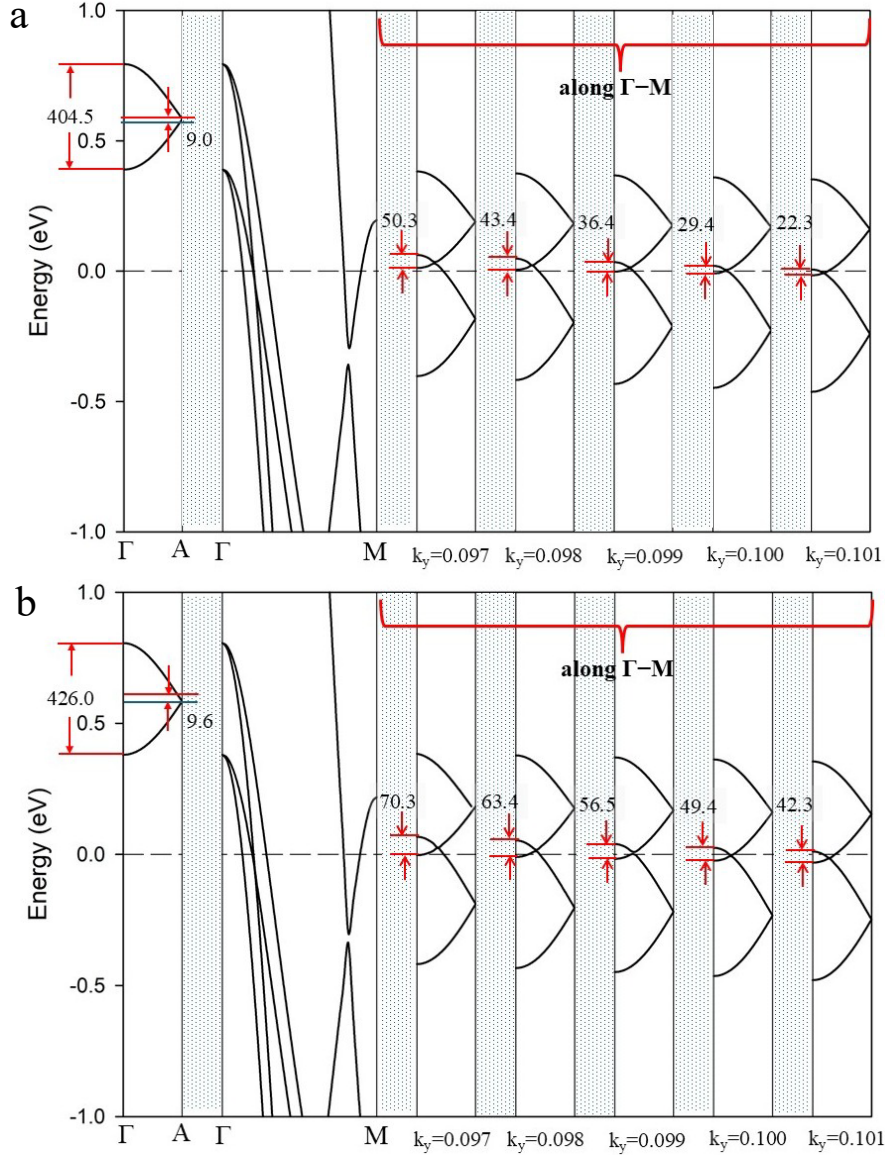


Figure 4. EBS for 2c superlattice of MgB₂ calculated using the LDA functional at (a) 4 GPa and (b) 8 GPa. Bands are calculated along lines that are between the light and heavy effective mass σ band Fermi surfaces, as shown in Figures 3 and 5. These bands refer to the distance from the origin (0, 0, 0) to the Brillouin zone boundary (at $k_y = 0.5$). Energy values for bands at Γ -A and Γ -M are meV; values for k_y are shown at bottom of figure for each segment along Γ -M.

Supplementary **Figure S1**, calculated for the $2c$ superlattice of MgB_2 using the GGA functional along the same directions shows that degenerate bands at Γ – A also split into two bands that cross near E_F . For the GGA calculation, bands at Γ follow a different trend to that shown in Figures 2 and 4 in that the “overlap” is minimal along Γ – M closer to Γ and leads to a separation of bands close to E_F at higher k_y values.

For completeness, **Figure S2** (Supporting Information) shows band structures at segments along Γ – M for values of $k_y < 0.091$ and $k_y > 0.101$. In the former case, the degenerate bands along Γ – A split into two bands with intersection above E_F . For the latter case, the bands are separate with no intersection or overlap at Γ . For $k_y \geq 0.124$, only the heavy effective mass bands intersect with E_F .

2.2.1. Corresponding Fermi surfaces at high pressure

Figure 5 shows the light and heavy effective mass Fermi surfaces for σ bands of the $2c$ superlattice for MgB_2 at 4 GPa and 8 GPa, respectively. Note that the folded light and heavy effective mass Fermi surfaces do intersect at 4 GPa and 8 GPa. This intersection is more apparent at 8 GPa, which also appears to develop an extended flat section on the outer side of the light effective mass Fermi surface and the inner side of the heavy effective mass Fermi surface (see region next to the bracket in Figure 5b).

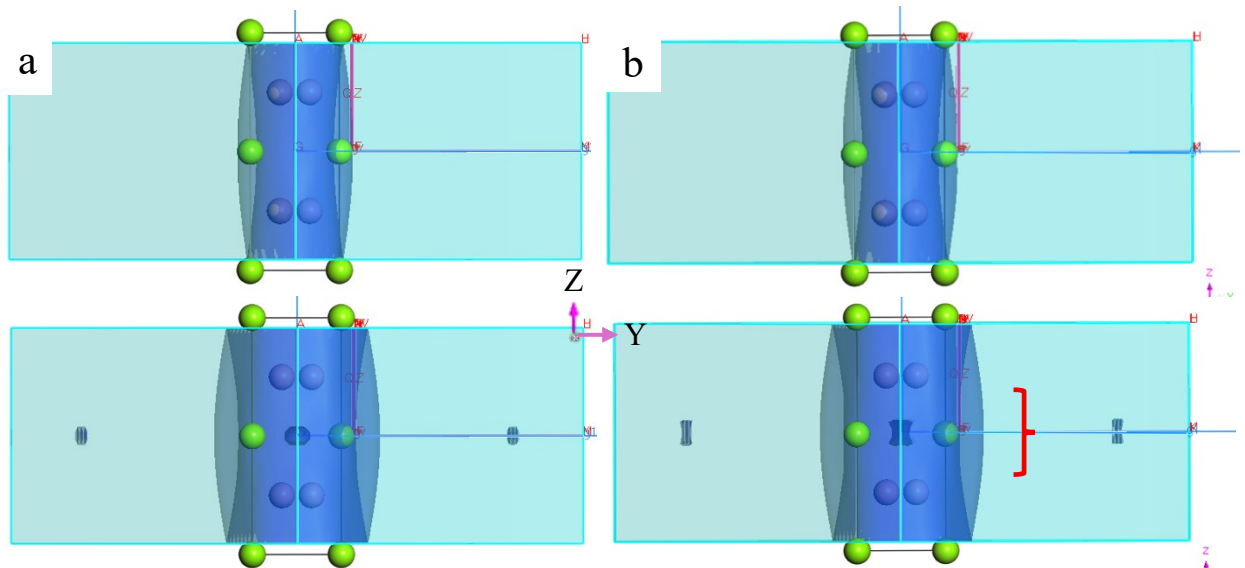


Figure 5. Fermi surfaces for the light (top) and heavy (bottom) effective masses σ bands of the $2c$ superlattice for MgB_2 (a) at 4 GPa and (b) at 8 GPa.

2.2.2. Fermi surfaces at other pressures

Figure 6 shows Fermi surfaces for the primitive cell of MgB_2 with increasing applied pressure. These Fermi surface calculations are used to graphically extract approximate coordinates for key points that enable analysis of band amplitudes (e.g. at the centre, inflection and Brillouin

zone boundary points). Fermi surfaces for the $1c$ primitive cell are used in order to reduce the clutter of folded Fermi surfaces that occur at higher pressures. A primitive cell facilitates graphical extraction of Fermi surface projected coordinates and enables correct attribution to light or heavy effective mass Fermi surface(s). The magnitudes of geometrical projections suggest that the folded Fermi surfaces have intersections. These geometrical values and intersections are discussed in more detail below and in Supporting Information.

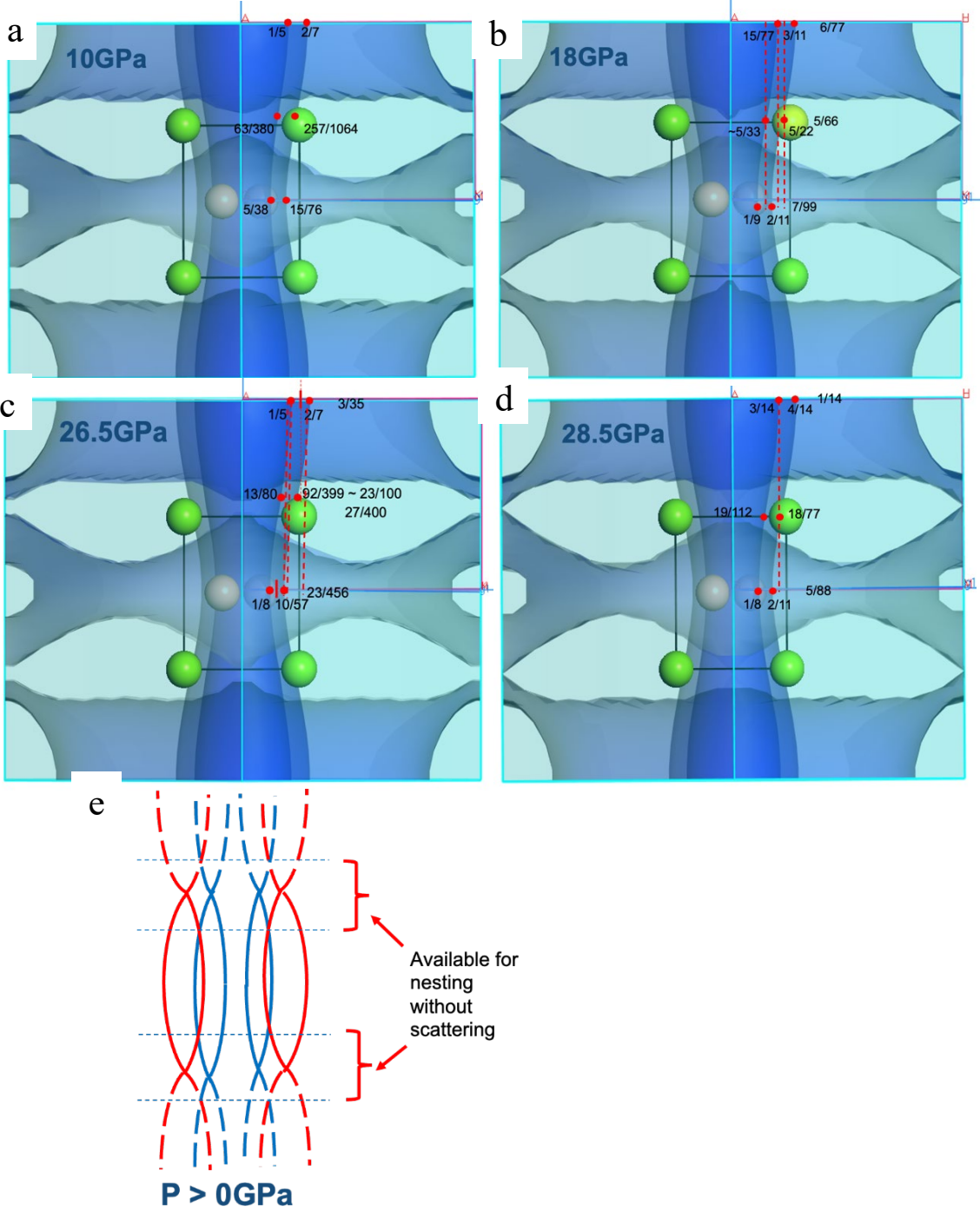


Figure 6. (a) Fermi surfaces for the light and heavy effective mass σ bands of the MgB₂ $1c$ primitive cell at (a) 10 GPa, (b) 18 GPa, (c) 26.5 and (d) 28.5 GPa. Figure 6e shows a schematic

of intersecting Fermi sections that occur upon folding at the inflection point with elevated pressure. Approximate coordinates of key intersection points (at the centre, inflection and Brillouin zone boundary points) of the projected Fermi surface are displayed as fractions of Γ –M.

3. Discussion

As is well known, electrons at the Fermi level in a narrow window of energies, of order the thermal energy, determine the electronic transport properties of solids.^[24, 25] For electrons with energy well below the Fermi level, significantly higher energies are required to excite these electrons into available empty electronic states. This requirement, based on Hund’s rules and Pauli’s principle, also applies to lowest energy empty states near the Fermi level. The interplay of electrons moving between filled and empty electronic states within a solid connected to two external electrodes facilitates electron transport between the electrodes. For this reason, the electron energies that are involved in transport phenomena belong to the narrow window of energy at the step transition of the Fermi-Dirac distribution (i.e. between fully populated and fully unpopulated electronic states below and above the Fermi level, respectively).

Typically, DFT calculations of electronic band structures are undertaken, and displayed, along high symmetry directions. In general, such two-dimensional representations are suitable measures of atomic-scale and bulk material properties based on characteristics and format of the displayed bands. Results shown in Figures 2 and 4 show that band characteristics for sections in close proximity to the Fermi surface (i.e. along directions parallel to Γ –A at regular intervals along Γ –M) can differ from that of bands along high symmetry directions.

The presence, or otherwise, of band degeneracy is a case to consider. For example, degenerate bands occur along Γ –A, but not for electronic bands along reciprocal directions closer to the Fermi surface where electrons/quasiparticles engaged in electronic transport properties reside. For the sections displayed in Figures 2 and 4 (along the Γ –M direction), degenerate bands only occur at the nodal point “A” for all pressures. Thus, degenerate electronic bands, generally expected to significantly impact physical properties of solids, may not always occur in close proximity to the Fermi surface.

3.1 Intra-band and inter-band hopping

As known from textbooks^[9, 11, 26] and demonstrated in earlier publications^[5, 27, 28], bands for a $2c$ superlattice can be geometrically constructed by folding bands that connect high symmetry nodes at the mid-point. This folding results in lens shaped cross-sections as shown in Figures 2 and 4. High resolution DFT calculations have also shown that the bonding and antibonding

sections of cosine shaped bands show asymmetry.^[5] This cosine band asymmetry, measured as a difference in energy, correlates well with the magnitude of the superconducting gap^[5, 27-29] and is mathematically described using corrected tight binding equations (1):

$$E^{H,L}(k_x, k_y, k_z) = E_0 - (2t_{\perp} - \Delta)\cos(ck_z) - \frac{\hbar^2}{2m^{H,L}} (k_x^2 + k_y^2) \quad 0 \leq ck_z \leq \pi/2 \quad (1)$$

$$E^{H,L}(k_x, k_y, k_z) = E_0 - (2t_{\perp} + \Delta)\cos(ck_z) - \frac{\hbar^2}{2m^{H,L}} (k_x^2 + k_y^2) \quad \pi/2 \leq ck_z \leq \pi$$

The degeneracy of the electronic bands along the Γ -A direction ($k_x, k_y = 0$), while not representative of electronic behaviour at the Fermi surface (as noted above), conveniently allows for identification of coincident tight binding equation parameters in (1). Similarly, evaluation of equation (1) on the respective light and heavy Fermi surfaces at their inflection points (i.e. $k_z = \pi/2c$ based on the $1c$ primitive unit cell) allows identification of energy equivalences at those points:

$$E_F = E(k_{Fx}^{H,L}, k_{Fy}^{H,L}, \pi/2c) = E_0 - \frac{\hbar^2}{2m^{H,L}} (k_{Fx}^{H,L^2} + k_{Fy}^{H,L^2}) \quad (2)$$

$$E_0 = E_F + \frac{\hbar^2}{2m^H} (k_{Fx}^H{}^2 + k_{Fy}^H{}^2) = E_F + \frac{\hbar^2}{2m^L} (k_{Fx}^L{}^2 + k_{Fy}^L{}^2)$$

Thus, even though the high symmetry direction Γ -A is not directly representative of electrons at the Fermi surface, convenient access to important coefficients of the tight binding equations is provided. In addition, the relations between light and heavy effective mass band coefficients can be determined. The equations at $k_x, k_y = 0$ also show that the Δ correction (in equation (1)) modulates a perfectly symmetric tight binding dependence with a cosine function.

3.2 Coupling of electron-hole pairs

The cosine modulated gap, combined with an absence of degeneracy for bands in proximity to the Fermi surface, are further indicators of a superconductivity mechanism. Mathematical analysis clarifying the conditions noted above have been discussed previously in the context of Bloch orbitals for an infinite linear chain with two s-states.^[9, 11, 15, 26] For the sake of clarity, we summarise key concepts below.

Two s-states per atom are considered hybridised on each atom, that is, the atomic contribution to the Bloch state for the linear chain is treated as a linear combination of the two atomic states. To construct the Bloch state for the linear chain, each hybridised atomic state is then multiplied by the exponential factor e^{ikma} and summed for all atoms in the linear chain. Crystal orbitals can also be constructed as linear combinations of the Bloch orbitals^[9, 10]

With use of the Schrödinger equation and projection onto each atomic state leads to a secular determinant for non-trivial solutions. Evaluation of the expression along the Γ -A direction ($k_x, k_y = 0$) takes the form:

$$\begin{vmatrix} E_0 - 2t_{\perp} \cos(ck_z) - E_k^H & \Delta \cos(ck_z) \\ \Delta \cos(ck_z) & E_0 - 2t_{\perp} \cos(ck_z) - E_k^L \end{vmatrix} = 0 \quad (3)$$

Equation (3) can be solved to obtain the k_z components of the equations shown in (1). The resulting bands are schematically displayed for a $1c$ primitive cell and an equivalent $2c$ superlattice in **Figures 7a and 7b**, respectively (compare Figure 7a to Figure 5.2 in^[26]).

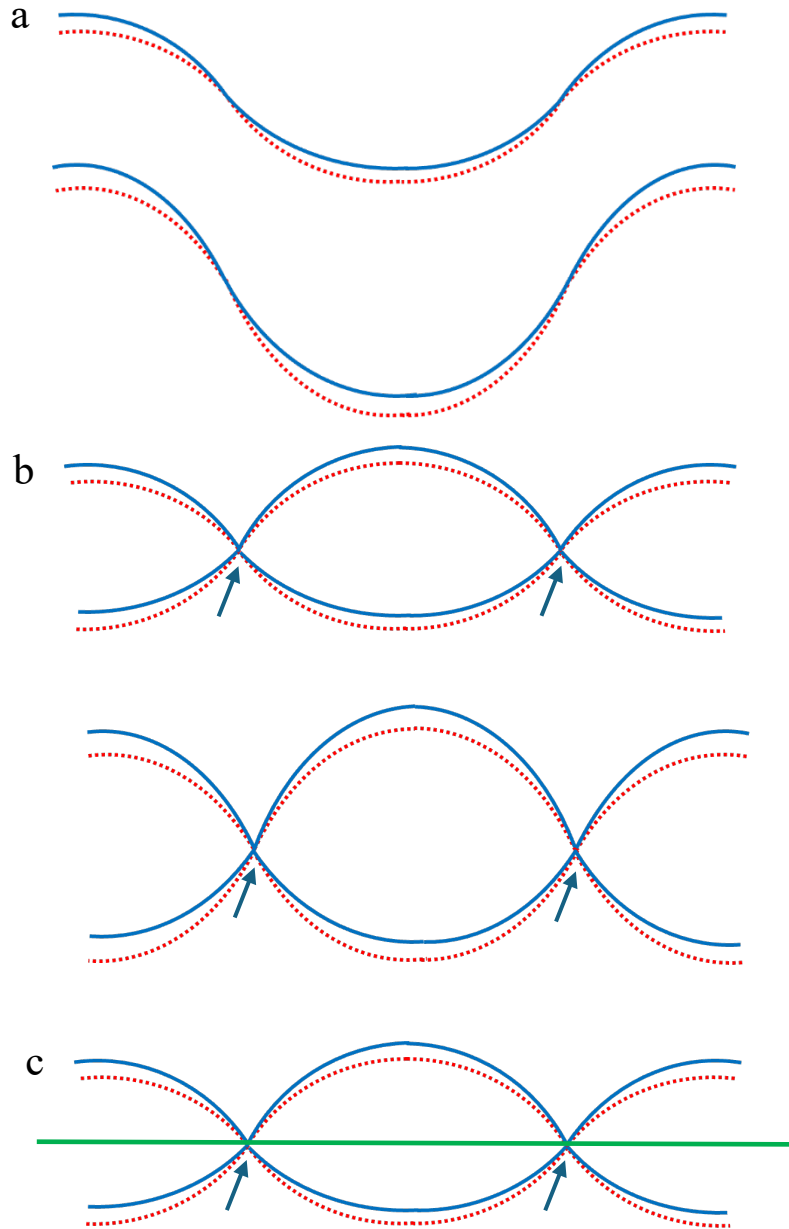


Figure 7. Schematic of cosine shaped MgB_2 electronic bands for (a) a $1c$ primitive unit cell, (b) a $2c$ superlattice, and (c) a $2c$ superlattice for bands aligned with the Fermi level (green line). The red dotted curves represent an electronic band in the absence of a hopping modulation of

Δ amplitude between the two different s states in adjacent atoms. The blue continuous curves include hopping between the two different states in adjacent atoms. Note that the red dotted and blue continuous curves have the same energy at the inflection mid-point $k_z = \pi/2c$ in Figure 7a. This aspect of band character becomes apparent in the folded representation shown in Figure 7b, where the point $k_z = \pi/2c$ (arrowed) becomes a nodal point.

The terms $2t_{\perp} \cos(ck_z)$ and $\Delta \cos(ck_z)$ correspond to ‘onsite’ matrix elements and hopping integrals between adjacent atoms, respectively. An intra-band excitation when using a cosine shaped band for the $1c$ primitive unit cell of MgB₂, becomes an inter-band excitation when using a folded cosine band for the $2c$ superlattice of MgB₂. Note that in the schematic of Figure 7, a cosine shaped band represents the cross-section of the Fermi surfaces shown in Figures 2 and 4.

Alignment of a nodal inflection point with the Fermi level occurs at axes parallel to the Γ -A direction that intersect the Fermi surface at $k_z = \pi/2c$, as shown in **Figure 7c** and Figure 2. This alignment, which closely resembles the electron and hole properties at, or in close vicinity of, the Fermi surface clearly indicates that a bonding-antibonding coupling between electrons and holes, can be activated. This concept is consistent with the picture of nesting identified from analysis of the topology of bands and Fermi surfaces when superlattices are used for calculations^[5]. Such nesting has been identified for sections of separate light and heavy effective mass σ Fermi surfaces. Since these nested regions are joined by respective (intra-) light and (intra-) heavy effective mass nesting vectors, the difference between these nesting vectors will also define inter-light and heavy σ Fermi surface nestings. In addition, alignment of a nodal inflection point with E_F is equivalent to electron-hole pair coupling and hybridisation concepts leading to gap formation at the nodal point, as previously described in the literature^[10]. We show that DFT calculations undertaken at high resolution carry key superconducting details, including mechanisms of electronic transport, because the calculations are not only for single electrons. Every time the geometry of a crystal is slightly modified during calculation, the electron density undergoes a redistribution to optimise, or minimize, energy. Therefore, responses to minor, or even sub-picometer, geometric changes are collective rather than individual or localised. As such, DFT appears to be better associated with ‘quasiparticle responses’ rather than individual electron behaviours. At the end of a geometry optimisation process, where minute geometry changes are required for convergence and the bands below the Fermi energy are nearly filled, we envisage that a redistribution of the last electron charge leaves behind a hole that the collective sea of adjacent electrons must accommodate.

3.3 Intersecting Fermi surfaces and band coherence

When DFT calculations show crossing of bands and Fermi surfaces with different slopes at the intersection, avenues or ‘pathways’ become available for electrons to change velocity or momentum. Such an intersection enables scattering, and loss of potential coherency. Coherent nesting has been previously identified for the folded Fermi surfaces of MgB₂, particularly at, and in the vicinity of, inflection points.^[5] These nesting regions become apparent when using $2c$ superlattices for DFT calculations but may remain unnoticed if working on a $1c$ primitive cell or higher symmetry configuration (e.g. P6/mmm). We note that the use of a $2c$ superlattice for DFT calculations of MgB₂ is inspired by experimental observation of superlattice peaks using Raman and synchrotron THz spectroscopies.^[12, 13]

The thermal energy carried by a collection of nearly free electrons is proportional to the number of electrons times the average thermal energy contributed through their degrees of freedom.^[24, 25] We posit that the volume fraction of Fermi surface where coherent nesting exists, before an intersection occurs (i.e. a different slope), will be proportional to the superconducting temperature. In other words, superconductivity is associated with the thermal energy that can be added to a system of coherent electrons before such coherency is destroyed.

The approximate position(s) of band crossing or intersection at various selected pressures can be calculated using relative distances extracted from graphical outputs for calculated Fermi surfaces. These positions have been estimated graphically for 10 GPa, 18 GPa, 26.5 GPa and 28.5 GPa using the calculated Fermi surfaces displayed on Figures 6a–6d, respectively, referring to key distances labelled on these figures. Further details on the calculations of key reciprocal distances are given in Supporting Information (**Table S1**).

These calculations result in respective fractions of 0.83457, 0.6688, 0.5206 and 0.4621 for the total (folded) k_z directions that can be nested before intersections that destroy coherency take place. By comparing these fractions of coherent nesting at pressure to that for MgB₂ at 0 GPa (i.e. a Fermi surface without band intersections), estimates for T_c at 10 GPa, 18 GPa, 26.5 GPa and 28.5 GPa, are 32.5 K, 26 K, 20.3 K and 18 K, respectively.

For reference, these estimated T_c values are shown in **Figure 8**, which compares experimentally determined T_c values as a function of pressure^[30, 31] and an alternative method to calculate T_c using the thermal energy of the well-known Kohn phonon anomaly.^[7] Noting that the graphical estimation of T_c in Figure 8 is less precise than some numerical methods because we have used additional indirect steps *via* image contrast and image resolution instead of using exact equations,^[32] the match with experimental values is good. The accuracy of estimates is improved at higher pressures because the intersections occur closer to inflection (nodal) points

of folded cosine shaped bands (where lower curvature is apparent). Higher mathematical accuracy could be achieved by using a function of the cosine dependence. However, the improvement is marginal and does not add significant value to the proof of this approach.

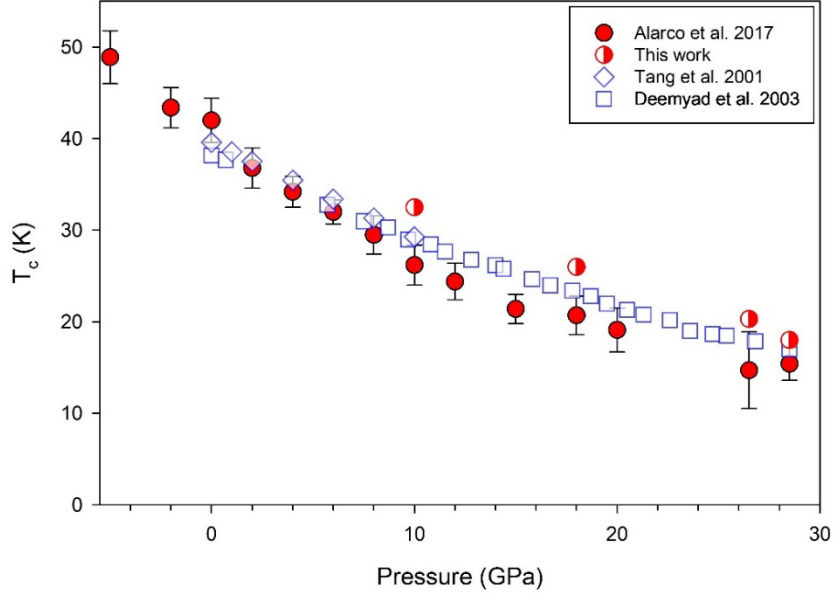


Figure 8. Estimated T_c based on calculated amplitudes of asymmetry for the cosine shaped band at the band intersection (half-filled symbols), compared with experimentally determined superconducting transition temperatures (open symbols)^[30, 31] and calculated values using changes to the Kohn anomaly in phonon dispersions (filled symbols)^[7]. Modified from Figure 2 of reference^[7].

3.4 Generality of approach

The approach described above for MgB_2 has common character with the topologies of other layered and non-layered superconducting compounds that display cosine-shaped electronic bands in close proximity to the Fermi level. For example, similar cosine shaped bands have been described for CaC_6 and LaH_{10} ^[27-29].

Tight binding equations for layered compounds are well known to result in cosine shaped bands.^[18, 19, 24, 25] The results shown above and in other studies^[5, 27-29] are strongly linked to the existence of cosine-shaped bands that show energy asymmetry correlated with the known energy gap. To date, superconducting cuprates have not been analysed for asymmetry of cosine shaped bands, although they are discernible in publications of previous DFT calculations.^[33, 34] Furthermore, the topology of the tubular shaped Fermi sections in many superconducting cuprates is favourable for nesting.

For superconducting solids of higher atomic number and greater element diversity, the required computational power will increase substantially. Accordingly, the resolution of DFT

calculations used in this work may not suit accurate determination of asymmetry, for example, with cuprate superconductors. Nevertheless, theoretical hopping models that include cosine dependence, have provided valuable insights on superconductivity for the high T_c cuprates.^[20, 21] Compelling evidence for a hopping mechanism can be identified using DFT-calculated, cosine shaped electronic bands that connect topological properties of these electronic bands and Fermi surfaces. While this discussion has focused on separate light and heavy effective mass σ bands and Fermi surfaces, the interplay between these bands *via* inter-band hopping is also likely to be present and relevant to superconducting mechanisms. This link between the geometry, or crystallography, of solids and their reciprocal space electronic properties at meV-scale is a key step towards predictable design of superconductors.

4. Conclusions

The electronic band structures of materials encompass a wealth of information on their potential superconductivity, which cannot be matched and extracted from approaches that focus only on using the density of states. A hopping mechanism associated with coherent nesting can be unequivocally identified from detailed analyses of cosine-shaped bands in the calculated electronic band structures of MgB_2 and other superconducting materials, when obtained using DFT with sufficiently high resolution.

The physics of superconductivity is determined by electrons within a narrow energy window at the Fermi surface. However, calculations are seldom undertaken at orientations adjacent to, or offset from, high symmetry directions. Examples are provided to show that the physics of electrons determining transport properties must be analysed with reference to calculations also along directions in proximity to the Fermi surface. A focus on the Fermi surface ensures an appropriate context for precise interpretation of physical and electronic behaviour.

Within the context of the Fermi surface geometry and topology, intersections of folded Fermi surfaces (calculated for $2c$ superlattices) and the corresponding electronic bands, add important criteria for the likely disruption of nested, coherent behaviour. The intersections, with significantly different slopes, provide avenues or ‘pathways’ for electrons from the nested collection to drastically change velocity or momentum, resulting in scattering.

This work demonstrates value adding to detailed interpretation of electronic properties by utilising the geometric characteristics of electronic bands and Fermi surfaces, routinely provided by DFT calculations. Our experimental observations of superlattices for MgB_2 are associated with the presence of cosine shaped bands and Fermi surface topologies favourable for nesting. The ubiquity of cosine-shaped bands in DFT calculations of superconductors and

strong correlations between cosine band asymmetry and the superconducting gap suggest that this systematic link may be more general than only for MgB₂.

The approach described above provides a cohesive and comprehensive view of superconductivity in reciprocal space using standard DFT calculated outputs that facilitates design and exploration of new compounds. To establish deterministic design criteria requires translation of systemic detail(s) on reciprocal space EBSs to real space bonding-antibonding orbital configurations matched to DFT algorithms. This challenge should enable design of next generation superconducting compounds with targeted properties, including room temperature transition.

5. Methods

DFT calculations on the EBS and FS for MgB₂ at pressures up to 30 GPa were undertaken with Materials Studio CASTEP Versions 2023 and 2025^[35] following procedures detailed in earlier publications.^[5, 7, 8] Key parameters such as plane wave cut-off energies, pseudopotentials, and $\Delta\mathbf{k}$ grids are critical enablers of meV resolution for EBS and PD calculations. All band structure representations utilize .xlsx files converted from direct .csv outputs of Materials Studio DFT calculations. These data are then re-plotted using SigmaPlot for Windows Version 15 (Grafiti LLC, Palo Alto, CA USA) to enable precise determination of band energies and intersections at reciprocal lattice symmetry points.

Band intersections with high symmetry points as well as bands close to, or at, Fermi surfaces are identified by graphical interpretation and re-plotted as compiled figures. Band degeneracy, splitting and/or band avoidances are determined by visual inspection of SigmaPlot graphs correlated with energy values to the fifth significant figure (i.e. < 1 meV). Precise interpretation of band intersections and/or avoidances can be obtained from DFT calculations undertaken with high resolution – a term used to describe the minimal input parameter values for DFT calculations as listed below.^[5, 8, 12] Examples of high resolution calculations showing evolution of bands along Γ –A with change in pressure are shown in **Figure S3** (Supporting Information). All DFT calculations employ cut-off energies of 990 eV, $\Delta\mathbf{k}$ grid of 0.005 Å⁻¹, norm-conserving pseudopotentials and either the Perdew-Zunger Local Density Approximation (LDA) or Generalised Gradient Approximation (GGA)^[36, 37] for the exchange-correlation functional. Electronic minimisation parameters include a total energy/atom convergence tolerance of 0.5 x 10⁻⁶ eV, an eigen-energy convergence tolerance of 0.1375 x 10⁻⁶ eV, a Fermi energy convergence tolerance of 0.2721 x 10⁻¹³ eV and a Gaussian smearing scheme of width 0.1 eV. Optimisation calculations use the Broyden-Fletcher-Goldfarb-Shannon (BFGS) algorithm employing a total energy convergence tolerance of 0.5 x 10⁻⁵ eV.

We have utilised superlattices to confirm experimental spectroscopic data,^[12, 13] to simplify computational methods for phonon dispersions of metal-substituted MgB₂,^[6, 38] as well as to calculate a superconducting gap using electronic band structures of MgB₂.^[5] Superlattice symmetry is maintained with a single primitive cell symmetry by the use of band folding in reciprocal space.^[39, 40] The folded topologies of the electronic bands and Fermi surfaces, corresponding to the superlattice, enable easier identification of electronic topological transitions and nesting relationships between extended sections of the Fermi surface.^[5]

Acknowledgements

The authors acknowledge the e-Research Office at QUT for access to high performance computing. During the preparation of this manuscript and study, the authors did not use any artificial intelligence tools.

Data Availability Statement

Additional data presented in this study are available in Supporting Information. Raw data files from DFT calculations are available from the authors on request.

Received: ((will be filled in by the editorial staff))

Revised: ((will be filled in by the editorial staff))

Published online: ((will be filled in by the editorial staff))

References

1. J. Kortus, Current progress in the theoretical understanding of MgB₂, *Physica C* **2007** 456 54–62.
2. J. M. An, W. E. Pickett, Superconductivity of MgB₂: Covalent bonds driven metallic, *Physical Review Letters* **2001** 86 19 4366–4369.
3. R. Heid, K. P. Bohnen, B. Renker, *Electron-phonon coupling and superconductivity in MgB₂ and related diborides*, Spring Meeting of the Deutsche-Physikalische-Gesellschaft Regensburg, Germany, 2002, pp. 293–305.
4. J. A. Alarco, P. C. Talbot, I. D. R. Mackinnon, Electron density response to phonon dynamics in MgB₂: an indicator of superconducting properties, *Mod. Numer. Sim. Mater. Sci.* **2018** 8 21–46.
5. J. A. Alarco, I. D. R. Mackinnon, Superlattices, Bonding-Antibonding, Fermi Surface Nesting, and Superconductivity, *Cond Matter* **2023** 8 72 1–13.
6. I. D. R. Mackinnon, P. C. Talbot, J. A. Alarco, Phonon dispersion anomalies and superconductivity in metal substituted MgB₂, *Comp. Mater. Sci.* **2017** 130 191–203.
7. J. A. Alarco, P. C. Talbot, I. D. R. Mackinnon, Phonon dispersion models for MgB₂ with application of pressure, *Physica C: Supercond Appl* **2017** 536 11–17.

8. I. D. R. Mackinnon, Almutairi A., J. A. Alarco, Insights from systematic DFT calculations on superconductors, in: Arcos, J.M.V. (Ed.), *Real Perspectives of Fourier Transforms and Current Developments in Superconductivity*, IntechOpen Ltd., London UK, **2021**, pp. 1–29.
9. E. Canadell, M.-L. Doublet, C. Lung, *Orbital Approach to the Electronic Structure of Solids*, Oxford University Press, Oxford, UK, **2012**.
10. E. Canadell, M. Whangbo, Conceptual aspects of structure property correlations and electronic instabilities, with applications to low-dimensional transition-metal oxides, *Chemical Reviews* **1991** 91 5 965–1034.
11. T. Albright, J. Burdett, M. Whangbo, *Orbital Interactions in Chemistry*, 2nd Edition ed., John Wiley & Sons, Inc. **2013**.
12. J. A. Alarco, A. Chou, P. C. Talbot, I. D. R. Mackinnon, Phonon Modes of MgB₂: Superlattice Structures and Spectral Response, *Phys Chem Chem Phys* **2014** 16 24443–24456.
13. J. A. Alarco, B. Gupta, M. Shahbazi, D. Appadoo, I. D. R. Mackinnon, THz/Far infrared synchrotron observations of superlattice frequencies in MgB₂, *Phys Chem Chem Phys* **2021** 23 41 23922–23932.
14. C. Buzea, T. Yamashita, TOPICAL REVIEW- Review of the superconducting properties of MgB₂, *Supercond. Sci. Technol.* **2001** 14 R115–R146.
15. M. Whangbo, S. Deng, J. Köhler, A. Simon, Interband Electron Pairing for Superconductivity from the Breakdown of the Born-Oppenheimer Approximation, *Chemphyschem* **2018** 19 23 3191–3195.
16. M. Whangbo, On the Relative Stability of the Metallic and the Insulating States of a Half-filled Band, *Journal of Chemical Physics* **1980** 73 8 3854–3861.
17. M. D. Johannes, I. I. Mazin, Fermi surface nesting and the origin of charge density waves in metals, *Phys. Rev. B* **2008** 77 16 165135.
18. I. N. Askerzade, Reviews of Topical Problems - Study of layered superconductors in the theory of an electron - phonon coupling mechanism, *Physics - Uspekhi* **2009** 52 10 977–988.
19. I. Askerzade, *Unconventional Superconductors - Anisotropy and Multiband Effects*, Springer-Verlag, Berlin Heidelberg, **2012**.
20. A. Mourachkine, *High-Temperature Superconductivity in Cuprates*, Kluwer Academic Publishers, Dordrecht, **2002**.
21. S.-i. Uchida, *High Temperature Superconductivity*, Springer, Tokyo Japan, **2015**.
22. W. Kohn, Nobel Lecture: Electronic structure of matter—wave functions and density functionals, *Rev. Modern Phys.* **1999** 71 5 1253–1266.
23. Y. Kong, O. V. Dolgov, O. Jepsen, O. K. Andersen, Electron-phonon interaction in the normal and superconducting states of MgB₂, *Phys. Rev. B* **2001** 64 020501 1–5.
24. N. W. Ashcroft, N. D. Mermin, *Solid State Physics*, Saunders, Philadelphia PA USA, **1976**.
25. P. Hofmann, *Solid State Physics: An Introduction*, Third ed., Wiley VCH, Berlin Germany, **2022**.
26. A. P. Sutton, *Electronic Structure of Materials*, Clarendon Press: Oxford Science Publications Oxford UK **2004**.
27. B. C. Wang, A. Bianconi, I. D. R. Mackinnon, J. A. Alarco, Superlattice Delineated Fermi Surface Nesting and Electron-Phonon Coupling in CaC₆, *Crystals* **2024** 14 499 1–17.

28. J. Alarco, I. Mackinnon, Spin Orbit Coupling for Superconductivity Models of LaH₁₀, *Annalen Der Physik* **2026** 538 1–17.
29. B. C. Wang, A. Bianconi, I. D. R. Mackinnon, J. A. Alarco, Superlattice Symmetries Reveal Electronic Topological Transition in CaC₆ with Pressure, *Crystals* **2024** 14 554 1–21.
30. J. Tang, L.-C. Qin, A. Matsushita, et al., Lattice parameter and T_c dependence of sintered MgB₂ superconductor on hydrostatic pressure, *Phys. Rev. B* **2001** 64 132509 1–4.
31. S. Deemyad, T. Tomita, J. Hamlin, et al., Dependence of the superconducting transition temperature of single and polycrystalline MgB₂ on hydrostatic pressure, *Physica C: Superconductivity* **2003** 385 1 105–116.
32. P. Malhotra, *Analytical Chemistry: Basic Techniques and Methods*, Springer Nature Switzerland AG, Cham, Switzerland, **2023**.
33. D. J. Singh, Electronic-structure of HgBa₂CuO₄, *Physica C* **1993** 212 1-2 228–232.
34. K. H. Bennemann, J. B. Ketterson, *The Physics of Superconductors: Volume II*, Springer Berlin, Heidelberg, Germany, **2004**.
35. S. J. Clark, M. D. Segall, C. J. Pickard, et al., First principles methods using CASTEP, *Z Kristallogr* **2005** 220 5-6 567–570.
36. J. P. Perdew, K. Burke, M. Ernzerhof, Generalized Gradient Approximation Made Simple, *Phys Rev Lett* **1996** 77 18 3865–3868.
37. J. P. Perdew, J. A. Chevary, S. H. Vosko, et al., Atoms, molecules, solids, and surfaces: Applications of the generalized gradient approximation for exchange and correlation, *Phys Rev B* **1992** 46 11 6671–6687.
38. J. A. Alarco, P. C. Talbot, I. D. R. Mackinnon, Phonon anomalies predict superconducting T_c for AlB₂-type structures, *Phys Chem Chem Phys* **2015** 17 38 25090–25099.
39. H. Jones, *The Theory of Brillouin Zones and Electronic States on Crystals*, North-Holland Publishing Company Amsterdam, **1960**.
40. S. L. Altmann, *Band Theory of Solids: An Introduction from the Point of View of Symmetry*, Clarendon Press, Oxford **2002**.

Supporting Information

Supporting Information is available from the authors.